Progress In Electromagnetics Research B, Vol. 36, 1–33, 2012

EFFECTIVE MATERIAL PROPERTY EXTRACTION OF A METAMATERIAL BY TAKING BOUNDARY EFFECTS INTO ACCOUNT AT TE/TM POLARIZED INCIDENCE

S. Kim[1, *], E. F. Kuester[2], C. L. Holloway[1], A. D. Scher[2], and J. R. Baker-Jarvis[1]

[1]National Institute of Standards and Technology, Electromagnetics Division, U.S. Department of Commerce, Boulder Laboratories, 325 Broadway, Boulder, CO 80305, USA

[2]Department of Electrical, Computer, and Energy Engineering, University of Colorado, 425 UCB, Boulder, CO 80309, USA

Abstract—In this paper, we present the extraction for effective material parameters for a metamaterial from TE or TM waveguide measurements with generalized sheet transition conditions (GSTCs) used to provide electric and magnetic surface susceptibilities that approximate boundary effects between the metamaterial and air. The retrieval algorithm determines the effective material properties via scattering data obtained from the metamaterial in a waveguide. The effective refractive index is expressed as a function of S-parameters for two samples of different length. The effective wave impedance is given in terms of S-parameters and the refractive index, assuming that GSTCs account for the boundary effects. The effective permittivity and permeability can then be determined through the refractive index and wave impedance. By use of S-parameters generated by commercial three-dimensional (3-D) full-wave simulation software our present equations are tested for two cases of metamaterials: magneto-dielectric ($\varepsilon_r = \mu_r$) and dielectric (TiO_2) particles. We also conduct S-parameter measurements on dielectric cubes with an S-band (WR-284) waveguide to compute the effective material properties. Furthermore, our results are compared to those derived from another retrieval method used in the literature, which does not account for boundary effects.

Received 29 July 2011, Accepted 22 September 2011, Scheduled 2 November 2011

* Corresponding author: Sung Kim (sung.x.kim@nist.gov).

1. INTRODUCTION

Since Pendry et al. demonstrated that a composite medium of periodically placed metallic wires can exhibit an effective negative permittivity [1] and metallic loop wires can show an effective negative permeability [2], a wide variety of metamaterial implementations and applications have been proposed. Based on the physical principle similar to the structure described in [2], spirals [3] and omega-shaped [4] metallic particles were considered to achieve artificial magnetic media. Taking advantage of resonance geometries different from those used in [1] and [2], recently studied metamaterials were composed of an array of magneto-dielectric spheres [5] or cubes [6, 7] and an array of dielectric cylinders with metallic patterns [8] to realize an isotropic effective dielectric and magnetic medium. Suggested potential applications of such metamaterials cover a broad range, such as a perfect lens [9], superlens [10], performance-improved antennas [11], and electromagnetic absorbers [12–14]. Metamaterials are therefore strategically applied in order to accomplish various design goals.

An embedded metamaterial has been also shown to be able to reduce the size of an electromagnetic device by shortening the resonance wavelength corresponding to its operational frequency. Miniaturization of cavity resonators was achieved by loading them with a metamaterial having a negative permittivity and permeability. This loading compensates for the wave propagation phase and artificially creates a longer wave propagation path than is possible with an ordinary material loading [15–18]. Alù et al. [19, 20] demonstrated that when a radiator is loaded with a metamaterial, the dispersion characteristics of a metamaterial, having negative parameters, can support efficient radiating modes, even if the radiator size is smaller than the free-space wavelength. Metamaterials can therefore be installed in various places in accordance with the design intended use. A metamaterial can be placed in a conducting cavity to miniaturize a device or at the aperture of a radiator to improve its radiation properties. A metamaterial can even be suspended in free space to control the direction of wave propagation.

Accurately determining the effective properties of a metamaterial is very important for design applications, because electromagnetic properties of metamaterials are fundamental to proper operation of a device. The conventional methods for extracting the effective properties of a metamaterial use S-parameters measured or simulated with a wave normally incident on the slab [21, 22]. Obtaining the S-parameters under the condition of actual metamaterial use is very important. To our knowledge, however, only a few papers have reported extraction of the effective properties of a metamaterial inserted into a rectangular waveguide [23–25], and adapted the same procedure as in [21, 22] (or with minor modifications), even though an electromagnetic wave no longer propagates normal to the metamaterial slab in the waveguide. These works also assumed, without any consideration of the boundary effects, that the Fresnel formulas that relate the reflection and transmission at the interface between the air and metamaterial are valid.

Cohn [26] attempted to model the boundary effects as a shunt susceptance to extract the refractive index of a medium composed of an arrangement of conducting obstacles. Later on, Brown and Jackson [27] investigated the reactive fields at interfaces between an artificial dielectric and air, regarding the artificial dielectric as a cascaded sequence of T-networks with the position of the effective interface being shifted. Scher and Kuester [28] used the point-dipole approximation and then applied the Clausis-Mossotti equations to compute the effective permittivity and permeability of a single-layer metamaterial. Independent of the above studies, Pekar [29] proposed the additional boundary condition (ABC) to properly treat macroscopic electromagnetic fields at the boundary, simply assuming that the polarization vanishes at the interface. Silveirinha et al. [30, 31] took advantage of the ABC for modeling an array of metallic wires. Simovski and Tretyakov [32, 33] extended Drude's model of a transition layer to extract the effective material parameters of a metamaterial. Vinogradov et al. [34] attempted to replace the transition layer by a "nonphysical" excess surface current to explain the jumps of the tangential component of macroscopic fields at the boundary.

In our previous paper [35], the case for an incident wave propagating normally towards a metamaterial slab was studied, taking the boundary effects into account, instead of making use of the Fresnel reflection and transmission coefficients that do not properly account for boundary effects. In this paper, we extend the equations in [35] to suit the case for a wave with oblique incidence. This will allow the measurements to be made in a rectangular waveguide. Similarly to [35], a metamaterial considered in this paper is assumed to be an isotropic and symmetrical medium, where the measured or simulated S-parameters are $S_{11} = S_{22}$ and $S_{21} = S_{12}$. We also postulate that the interfaces obey reciprocity; i.e., the air-to-slab and slab-to-air transmissions are the same. Without assuming the Fresnel reflection and transmission coefficients, we present the equation for determining the effective refractive index of a metamaterial as a function of air-to-slab and slab-to-air reflections and transmission that can be found from the S-parameters, either measured or simulated by two samples of different length. The formulation in this paper appears very analogous to the line-reflect-line (LRL) method [36–39].

Furthermore, as in [35], we assume in this work that the reflection and transmission coefficients are related only through generalized sheet transition conditions (GSTCs). Kuester et al. [40] have studied the average transition conditions for the electromagnetic field across a metafilm (two-dimensional metamaterial made of a planar array of scatterers). The surface distribution of the scatterers is replaced by a continuous distribution of the electric and magnetic surface susceptibilities in the surface. The final expressions of the GSTCs involve the average (macroscopic) electric and magnetic fields on either side of the interface between a metamaterial and air, and can be used to give the relation of the electric and magnetic surface susceptibilities to the reflection and transmission coefficients at the interface. Scher and Kuester [41] explained that GSTCs of this type govern the macroscopic fields at the interface. This means that the jumps of macroscopic fields at the boundary are expressed by effective electric and magnetic susceptibilities found from the GSTCs. In this paper, we determine the effective refractive index of a metamaterial from the S-parameter data for two samples of different length. We then take into account the boundary effects due to the excess polarization and magnetization induced at the interface, which are approximated by electric and magnetic susceptibilities, to derive the equation that extracts the effective wave impedance of a metamaterial for the case of a wave impinging obliquely on a metamaterial slab. The effective permittivity and permeability of a metamaterial can then readily be found from the effective refractive index and wave impedance.

To validate our equations presented here, two metamaterials will be examined; one for the case when the permittivity and permeability of magneto-dielectric cubic particles for the metamaterial in a waveguide are the same ($\varepsilon_r = \mu_r$), and the other for the case where dielectric (TiO_2) cubes ($\varepsilon_r \neq \mu_r$) are arranged. In the first case, the effective material properties of the metamaterial will be extracted from the S-parameters simulated for TE and TM polarizations. In the latter case, we will attempt to retrieve the material parameters from the S-parameters simulated for TE and TM cases and experimentally measured by an S-band (WR-284) waveguide holding the dielectric cubes. For both first and second metamaterial configurations, our results are discussed by comparison to those obtained from the extraction method [25] which does not account for the boundary effects occurring between a metamaterial and air.

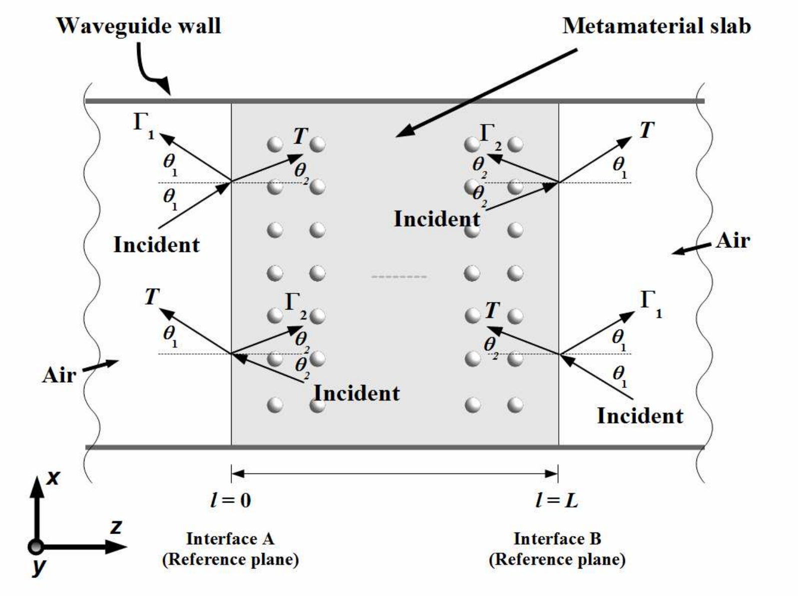

Figure 1. Schematic illustration of the incidence, reflection, and transmission on a metamaterial in a waveguide under test.

2. EQUATIONS FROM *S*-PARAMETERS OF TWO SAMPLES OF DIFFERENT LENGTHS

The structure shown in Figure 1 represents a metamaterial sample placed in a waveguide along with the reflection and transmission of electromagnetic waves obliquely incident on the metamaterial. A wave incident from the air to the metamaterial with incidence angle θ_1 is refracted at an angle θ_2 by the interface A, whereas a wave propagating from the metamaterial to the air is incident at an angle θ_2 and refracted at θ_1 by the interface B. In Figure 1, Γ_1 is the reflection coefficient that relates the tangential components of the incident and reflected waves in the air, Γ_2 is the reflection coefficient in the metamaterial, and T is the transmission coefficient that relates the tangential components of the incident and transmitted waves. As in [35], the interfaces A and B are regarded as reciprocal but asymmetrical networks; Γ_1 and Γ_2 are not necessarily the same, and T is equal in both propagation directions (here, T is just a transmission of the S-parameters and is not a field amplitude ratio). Note that in this paper, these coefficients are not assumed to be related to the bulk material parameters of a metamaterial by the Fresnel formulas. The metamaterial sample in Figure 1 can be viewed as a two port characterized by the S-parameters observed at the interfaces A and B. Similar to the normal-incidence case in [35], we assume that $S_{11} = S_{22}$ and $S_{21} = S_{12}$, the S-parameters can then be expressed as

$$S_{11} = \Gamma_1 + tS_{21}\Gamma_2 \tag{1}$$

$$S_{21} = \frac{tT^2}{1-(t\Gamma_2)^2}, \tag{2}$$

where

$$t = \exp\left[-j\sqrt{\frac{\omega^2 \varepsilon_{r,\mathit{eff}}\,\mu_{r,\mathit{eff}}}{c^2} - \left(\frac{2\pi}{\lambda_c}\right)^2}\,L\right] = \exp\left[-j\frac{2\pi L}{\Lambda}\right]. \tag{3}$$

In Equations (1)–(3), S_{11} and S_{21} are measured or simulated S-parameters, $\varepsilon_{r,\mathit{eff}}$ and $\mu_{r,\mathit{eff}}$ are the effective relative permittivity and permeability of the metamaterial in a waveguide, c is the speed of light in air, and λ_c is the cutoff wavelength for the dominant mode in the air-filled region of the waveguide, e.g., TE_{10} for a metallic rectangular waveguide. In Equation (3), L is the slab length of the metamaterial, defined as $L = Na$ in this paper, where N is the number of unit cells and a is the size of each unit cell in the propagation direction. Λ is the guide wavelength within the metamaterial slab placed in a waveguide, and $1/\Lambda^2$ is given by

$$\frac{1}{\Lambda^2} = \frac{\varepsilon_{r,\mathit{eff}}\,\mu_{r,\mathit{eff}}}{\lambda_0^2} - \frac{1}{\lambda_c^2} = -\left(\frac{1}{2\pi L}\ln\frac{1}{t}\right)^2, \tag{4}$$

where λ_0 is the wavelength in air. Note that (4) has an infinite number of branches, since the angle of a complex value of $1/t$ is equal to the principal branch of this complex value plus $2\pi m$, where m is an integer.

We can also explicitly find Γ_1, Γ_2 and T^2 from Equations (1)–(3) by use of the S-parameters measured or simulated by two samples of different length, $L = L1$ and $L2$, as follows:

$$\Gamma_1 = \frac{-X \pm \sqrt{X^2 - 4\left(S_{11}^{L1} - S_{11}^{L2}\right)^2 Y}}{2\left(S_{11}^{L1} - S_{11}^{L2}\right)}, \tag{5}$$

where

$$X = -\left(S_{11}^{L1}\right)^2 + \left(S_{11}^{L2}\right)^2 + \left(S_{21}^{L1}\right)^2 - \left(S_{21}^{L2}\right)^2 \tag{6}$$

$$Y = \left(S_{11}^{L1}\right)^2 S_{11}^{L2} - S_{11}^{L1}\left(S_{11}^{L2}\right)^2 + S_{11}^{L1}\left(S_{21}^{L2}\right)^2 - \left(S_{21}^{L1}\right)^2 S_{11}^{L2} \tag{7}$$

and

$$t^{L1}\Gamma_2 = \frac{S_{11}^{L1} - \Gamma_1}{S_{21}^{L1}}, \tag{8}$$

$$t^{L1}T^2 = S_{21}^{L1}\left\{1 - \left(\frac{S_{11}^{L1} - \Gamma_1}{S_{21}^{L1}}\right)^2\right\} = S_{21}^{L1}\left\{1 - \left(t^{L1}\Gamma_2\right)^2\right\}. \tag{9}$$

In the above equations, the superscripts $L1$ and $L2$ denote the parameters measured or computed from the samples of length $L1$ and $L2$, respectively. If $L1$ is replaced by $L2$ in Equations (8) and (9), the equations still hold true. Note that Equation (5) produces two possible solutions. In the case when a material is passive, the physical requirement $|\Gamma_1| \leq 1$ fixes the choice of the sign. However, the same cannot necessarily be applied to Γ_2 when the material is very lossy [42].

We can also solve Equations (1)–(4) for the refractive index, if the S-parameter data are available for the samples of length $L1$ and $L2$:

$$\begin{aligned} n_{\mathit{eff}} &= \pm\sqrt{\varepsilon_{r,\mathit{eff}}\,\mu_{r,\mathit{eff}}} \\ &= \pm\lambda_0\sqrt{\frac{1}{\lambda_c^2} - \left\{\frac{1}{2\pi(L2-L1)}\left[\ln\left\{\frac{S_{21}^{L2}\left(S_{11}^{L1}-\Gamma_1\right)}{S_{21}^{L1}\left(S_{11}^{L2}-\Gamma_1\right)}\right\} + j2\pi m\right]\right\}^2}, \end{aligned} \tag{10}$$

where m is an integer. The sign ambiguity in the above equation can be resolved by $\mathrm{Im}\,(n_{\mathit{eff}}) \leq 0$ if the metamaterial inclusions are passive. When varying the integer m in Equation (10) and inserting Equation (10) to Equation (4), the integer ambiguity can be resolved by forcing the group delay calculated by $L \cdot [\frac{d(1/\Lambda)}{df}]$ from Equation (4) to match the experimentally or numerically obtained group delay for the sample length. For this method to work, the permittivity and permeability of the material need to change by only a small amount at each discrete frequency point for which the group delay is calculated. A metamaterial for measurement or simulation that has a very dispersive characteristic may still cause difficulty in addressing the integer ambiguity. In order to work around this problem, we have attempted to minimize the discrepancies of multiple refractive indices from some combinations of different-length samples; i.e., 2 and 3 layers, 2 and 4 layers, and 3 and 4 layers, assuming that the samples possess identical properties.

In our approach so far, we notice that the formulations are very similar to the line-reflect-line (LRL) method that is often used as a calibration technique for vector network analyzers (VNAs) [36] or can even be used to extract the transmission line characteristics [37–39] by use of two different delay lines. Our equations presented here are understood, because the interfaces A and B in Figure 1 can be viewed as the error boxes or discontinuities in [36–39].

Most metamaterials show very lossy characteristics in certain bands, and S_{21} becomes very small near the resonances. In that case, our present equations may be too sensitive to the S-parameters. Similarly to [35], instead of immediate use of Equations (5) and (8), we can use the following alternative expressions for Γ_1 and $t^{L1}\Gamma_2$:

$$\begin{aligned}\Gamma_1 =& S_{11}^{av} - S_{21}^{av}\frac{\Delta S_{21}}{\Delta S_{11}}\\ &\pm\frac{\Delta S_{11}}{2}\sqrt{\left\{1-\left(\frac{\Delta S_{21}}{\Delta S_{11}}\right)^2\right\}\left\{1-4\left(\frac{S_{21}^{av}}{\Delta S_{11}}\right)^2\right\}}\end{aligned} \tag{11}$$

$$t^{L1}\Gamma_2 = \frac{\frac{S_{21}^{av}}{\Delta S_{11}}+\frac{\Delta S_{21}}{2\Delta S_{11}}}{\frac{1}{2}+\frac{S_{21}^{av}\Delta S_{21}}{(\Delta S_{11})^2}\pm\frac{1}{2}\sqrt{\left\{1-\left(\frac{\Delta S_{21}}{\Delta S_{11}}\right)^2\right\}\left\{1-4\left(\frac{S_{21}^{av}}{\Delta S_{11}}\right)^2\right\}}}, \tag{12}$$

which are functions of differences and averages of S-parameters:

$$\begin{aligned}\Delta S_{11} &= S_{11}^{L1} - S_{11}^{L2}\\ \Delta S_{21} &= S_{21}^{L1} - S_{21}^{L2}\\ S_{11}^{av} &= \frac{S_{11}^{L1}+S_{11}^{L2}}{2}\\ S_{21}^{av} &= \frac{S_{21}^{L1}+S_{21}^{L2}}{2}.\end{aligned} \tag{13}$$

The ± sign in Equation (11) is determined in the same way as in Equation (5). The choice of the sign in Equation (12) is the same as that in Equation (11). $t^{L1}T^2$ is calculated by substituting Equation (12) into Equation (9). When the squared ratios $(\Delta S_{21}/\Delta S_{21})^2$ and $(S_{21}^{av}/\Delta S_{11})^2$ are much smaller than unity, then the square roots in (11) and (12) can be approximated to unity.

3. EQUATIONS FROM GENERALIZED SHEET TRANSITION CONDITIONS (GSTCS)

3.1. GSTCs in the TE Case

The relation of the reflection and transmission at the interface between an ordinary material and metamaterial is required for property extraction techniques of any kind. Together with the S-parameter measurements or simulations of samples of two different lengths, we

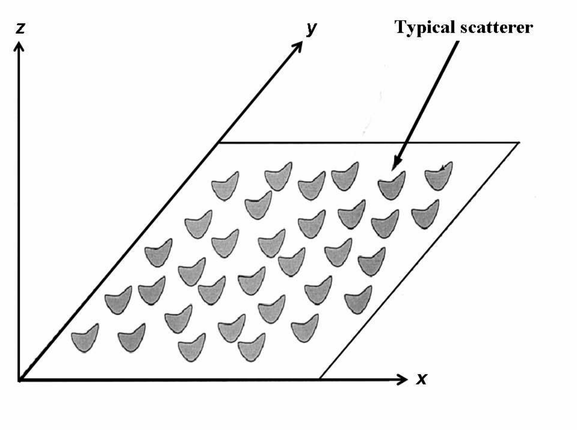

Figure 2. 2-D metamaterial in x-y plane.

use the GSTCs to relate the reflections Γ_1, Γ_2, and transmission T. In [40], for the averaged transition conditions of the macroscopic electromagnetic fields over a metafilm (two-dimensional metamaterial sheet), the classical boundary conditions have been considered to apply. The transition boundary conditions at the interface between an ordinary material and metafilm have been expressed in terms of the effective surface susceptibilities of the metafilm. The expressions of the conditions have appeared to be the GSTCs of second order and been employed to relate the reflection and transmission at the boundary, taking into account the boundary effects caused by the polarization and magnetization induced at the metafilm composed of scatterers. In Figure 2, the GSTCs are given by

$$\vec{a}_z \times \vec{H}\Big|_{z=0-}^{0+} = j\omega\varepsilon_0 \overleftrightarrow{\chi}_{ES} \cdot \vec{E}_{t,av}\Big|_{z=0} - \vec{a}_z \times \nabla_t \left[\chi_{MS}^{zz} \frac{B_{z,av}}{\mu}\right]_{z=0} \tag{14}$$

$$\vec{E}\Big|_{z=0-}^{0+} \times \vec{a}_z = j\omega\mu_0 \overleftrightarrow{\chi}_{MS} \cdot \vec{H}_{t,av}\Big|_{z=0} - \nabla_t \left[\chi_{ES}^{zz} \frac{D_{z,av}}{\varepsilon}\right]_{z=0} \times \vec{a}_z, \tag{15}$$

where $\vec{D}_{av}$ and $\vec{B}_{av}$ are the average electric and magnetic flux densities, and $\overleftrightarrow{\chi}_{ES}$ and $\overleftrightarrow{\chi}_{MS}$ are the effective electric and magnetic susceptibilities given respectively by the diagonal dyadics,

$$\overleftrightarrow{\chi}_{ES} = \chi_{ES}^{xx}\vec{a}_x\vec{a}_x + \chi_{ES}^{yy}\vec{a}_y\vec{a}_y + \chi_{ES}^{zz}\vec{a}_z\vec{a}_z \tag{16}$$

$$\overleftrightarrow{\chi}_{MS} = \chi_{MS}^{xx}\vec{a}_x\vec{a}_x + \chi_{MS}^{yy}\vec{a}_y\vec{a}_y + \chi_{MS}^{zz}\vec{a}_z\vec{a}_z. \tag{17}$$

Also, Mohamed et al. [43] reported that electric dipoles embedded in the interface between two media produce different related effective surface susceptibilities, depending on the orientations of the dipoles. We can therefore deduce that consideration of the polarizations of an incident wave would be significant in applying Equations (14) and (15) to find the effective surface susceptibilities.

Consider a TE polarized plane wave incident from air ($z < 0$) to the metamaterial ($z > 0$), assuming the interface A to be located at $z = 0$. The total electric field $\vec{E}$ at $z < 0$ is given by summing the incident and reflected electric fields $\vec{E^i}$ and $\vec{E^r}$, where

$$\begin{aligned}\vec{E} &= \vec{E^i} + \vec{E^r},\\ \vec{E^i} &= \vec{a}_y E_0 e^{-j\vec{k}_i\cdot\vec{r}}\\ \vec{E^r} &= \vec{a}_y \Gamma_1 E_0 e^{-j\vec{k}_r\cdot\vec{r}}.\end{aligned} \tag{18}$$

where $\vec{r} = x\vec{a}_x + y\vec{a}_y + z\vec{a}_z$. Likewise, at $z < 0$, the total magnetic field $\vec{H}$ is expressed in terms of the incident and reflected magnetic fields $\vec{H^i}$ and $\vec{H^r}$, where

$$\begin{aligned}\vec{H} &= \vec{H^i} + \vec{H^r},\\ \vec{H^i} &= \frac{E_0}{\zeta_0}\left(-\vec{a}_x\cos\theta_1 + \vec{a}_z\sin\theta_1\right)e^{-j\vec{k}_i\cdot\vec{r}}\\ \vec{H^r} &= \frac{\Gamma_1 E_0}{\zeta_0}\left(\vec{a}_x\cos\theta_1 + \vec{a}_z\sin\theta_1\right)e^{-j\vec{k}_r\cdot\vec{r}},\end{aligned} \tag{19}$$

where ζ_0 is the wave impedance of air. In addition, at $z > 0$, the transmitted electric and magnetic fields $\vec{E^t}$ and $\vec{H^t}$ are

$$\vec{E^t} = \vec{a}_y T_1 E_0 e^{-j\vec{k}_t\cdot\vec{r}} \tag{20}$$

$$\vec{H^t} = \frac{T_1 E_0}{\zeta_{\mathit{eff}}^{\mathrm{TE}}}\left(-\vec{a}_x\cos\theta_2 + \vec{a}_z\sin\theta_2\right)e^{-j\vec{k}_t\cdot\vec{r}}, \tag{21}$$

where $\zeta_{\mathit{eff}}^{\mathrm{TE}}$ is the effective absolute wave impedance of a metamaterial of the TE mode. In Equations (20) and (21), T_1 is not the same as T in Figure 1, but is rather the amplitude ratio of the field transmitted into the metamaterial and the field incident from the air, where $T_1 = T\sqrt{(\zeta_{\mathit{eff}}^{\mathrm{TE}}\cos\theta_1)/(\zeta_0\cos\theta_2)}$. In Equations (18)–(21), the wavenumbers are given by

$$\begin{aligned}\vec{k_i} &= \left(\vec{a}_x\sin\theta_1 + \vec{a}_z\cos\theta_1\right)k_0\\ \vec{k_r} &= \left(\vec{a}_x\sin\theta_1 - \vec{a}_z\cos\theta_1\right)k_0\\ \vec{k_t} &= \left(\vec{a}_x\sin\theta_2 + \vec{a}_z\cos\theta_2\right)k_{\mathit{eff}}^{\mathrm{TE}},\end{aligned} \tag{22}$$

where k_0 is the wavenumber of air and $k_{\mathit{eff}}^{\mathrm{TE}}$ is the effective wavenumber of a metamaterial of the TE mode.

Substitution of Equations (18)–(21) into Equation (15) by use of the total electric flux density $\vec{D} = \varepsilon_0 \vec{E^i} + \varepsilon_0 \vec{E^r}$ at $z < 0$ and the transmitted electric flux density $\vec{D^t} = \varepsilon_{\mathit{eff}}^{\mathrm{TE}} \vec{E^t}$ at $z > 0$ ($\varepsilon_{\mathit{eff}}^{\mathrm{TE}}$ is the effective absolute permittivity of the metamerial) results in the effective magnetic surface susceptibilities at the interface A:

$$\chi_{MS,A}^{xx} = -\frac{T\sqrt{\frac{\zeta_{\mathit{eff}}^{\mathrm{TE}}\cos\theta_1}{\zeta_0\cos\theta_2}} - (1+\Gamma_1)}{\frac{j\omega\mu_0}{2}\left\{\frac{1-\Gamma_1}{\zeta_0}\cos\theta_1 + T\sqrt{\frac{(\cos\theta_1)(\cos\theta_2)}{\zeta_0\zeta_{\mathit{eff}}^{\mathrm{TE}}}}\right\}}, \tag{23}$$

with

$$\cos\theta_1 = \sqrt{1-(f_c/f)^2} \tag{24}$$

$$\cos\theta_2 = \sqrt{1-\{f_c/(n_{\mathit{eff}} f)\}^2}, \tag{25}$$

where f is the operating frequency and f_c is the cutoff frequency of the waveguide. In addition, considering a TE polarized plane wave transmitted from the metamaterial ($z > 0$) to the air ($z < 0$) leads to the effective magnetic surface susceptibilities at the interface B:

$$\chi_{MS,B}^{xx} = -\frac{T\sqrt{\frac{\zeta_0\cos\theta_2}{\zeta_{\mathit{eff}}^{TE}\cos\theta_1}} - (1+\Gamma_2)}{\frac{j\omega\mu_0}{2}\left\{\frac{1-\Gamma_2}{\zeta_{\mathit{eff}}^{\mathrm{TE}}}\cos\theta_2 + T\sqrt{\frac{(\cos\theta_1)(\cos\theta_2)}{\zeta_0\zeta_{\mathit{eff}}^{\mathrm{TE}}}}\right\}}. \tag{26}$$

The effective surface susceptibilities in Equations (23) and (26) are those for the semi-infinite metamaterial slab. Therefore, the slab length of the metamaterial under investigation must be large enough that near-field interaction is negligible. If we assume that the effective surface susceptibilities induced at each interface are the same, i.e., $\chi_{MS,A}^{xx} = \chi_{MS,B}^{xx}$, then we obtain the expression for the effective wave impedance of the metamaterial from Equations (23) and (26):

$$\zeta_{\mathit{eff}}^{\mathrm{TE}} = \sqrt{\frac{\mu_{r,\mathit{eff}}^{\mathrm{TE}}}{\varepsilon_{r,\mathit{eff}}^{\mathrm{TE}}}}\zeta_0 = \frac{\left\{(1+\Gamma_1)(1-\Gamma_2)+T^2\right\}\cos\theta_2}{\left\{(1-\Gamma_1)(1+\Gamma_2)+T^2\right\}\cos\theta_1}\zeta_0. \tag{27}$$

Note that for the normal incidence, $\theta_1 = \theta_2 = 0$, Equation (27) is reduced simply to Equation (11) in [35].

Moreover, the effective relative permittivity and permeability are calculated from $n_{\mathit{eff}}/(\zeta_{\mathit{eff}}/\zeta_0)$ and $n_{\mathit{eff}} \cdot (\zeta_{\mathit{eff}}/\zeta_0)$. From Equations (10) and (27), we have

$$\varepsilon_{r,\mathit{eff}}^{\mathrm{TE}}=\pm\frac{\lambda_0\sqrt{\frac{1}{\lambda_c^2}-\left\{\frac{1}{2\pi(L2-L1)}\left[\ln\left\{\frac{S_{21}^{L2}\left(S_{11}^{L1}-\Gamma_1\right)}{S_{21}^{L1}\left(S_{11}^{L2}-\Gamma_1\right)}\right\}+j2\pi m\right]\right\}^2}}{\dfrac{\left\{(1+\Gamma_1)\left(1-\Gamma_2\right)+T^2\right\}\cos\theta_2}{\left\{(1-\Gamma_1)\left(1+\Gamma_1\right)+T^2\right\}\cos\theta_1}} \tag{28}$$

and

$$\mu_{r,\mathit{eff}}^{\mathrm{TE}}=\pm\lambda_0\sqrt{\frac{1}{\lambda_c^2}-\left\{\frac{1}{2\pi(L2-L1)}\left[\ln\left\{\frac{S_{21}^{L2}\left(S_{11}^{L1}-\Gamma_1\right)}{S_{21}^{L1}\left(S_{11}^{L2}-\Gamma_1\right)}\right\}+j2\pi m\right]\right\}^2}\cdot\frac{\left\{(1+\Gamma_1)\left(1-\Gamma_2\right)+T^2\right\}\cos\theta_2}{\left\{(1-\Gamma_1)\left(1+\Gamma_1\right)+T^2\right\}\cos\theta_1}. \tag{29}$$

The ± signs in Equations (28) and (29) are congruent according to the choice of sign in Equation (10).

The equations for the effective material properties are given by Equations (10), (27), (28), and (29). The material parameter extraction method presented in this paper is based on measured or simulated S-parameter data from two samples of different length, which allows us to determine the effective material parameters of metamaterial without the need for information on the interior of the sample. To make these equations valid and make them work accurately, we should make sure that there are enough layers in each sample for the metamaterial to exhibit well-converged effective properties. The homogenization limit, $|k_0 n_{\mathit{eff}}\, a| < 1$, must also be satisfied (see [28]).

Our assumption has been that the metamaterial can be modeled as an isotropic effective medium. This should certainly be true for a metamaterial made of isotropic spheres or cubes, as we will consider below. In such a case, all modes of the metamaterial-filled waveguide should still be TE or TM, though this will not necessarily be true of more complicated metamaterials such as those based on split-ring resonators. Another point to be taken into account is that, when the effective parameters of the metamaterial are large enough, higher order modes may be above cutoff in the loaded section of waveguide. In contrast, however, the measurement by means of a network analyzer with excitation by the dominant mode (TE_{10}) mode in an air-filled waveguide will detect only the dominant mode. It is assumed that all higher-order modes that arise at the interfaces are evanescent and sufficiently decay at the input and output ports of the waveguide as long as the air-filled regions of the waveguide are long enough in the wave propagation direction. If higher-order modes do not decay in the loaded section of guide, mode conversion may make the model we have employed inaccurate, and a more elaborate model would have to be used. Our algorithm in its present form is based on the simplifying assumptions listed above.

3.2. GSTCs in the TM Case

Consider a TM wave incident from air ($z < 0$) to the metamaterial slab ($z > 0$), such that the total, incident, and reflected magnetic fields at $z < 0$ are given by

$$\begin{aligned}\vec{H} &= \vec{H}^i + \vec{H}^r,\\ \vec{H}^i &= \frac{E_0}{\zeta_0}\vec{a}_y e^{-j\vec{k}_i\cdot\vec{r}}\\ \vec{H}^r &= \frac{\Gamma_1 E_0}{\zeta_0}\left(-\vec{a}_y\right) e^{-j\vec{k}_i\cdot\vec{r}}.\end{aligned} \tag{30}$$

The total, incident, and reflected electric fields at $z < 0$ are

$$\begin{aligned}\vec{E} &= \vec{E}^i + \vec{E}^r,\\ \vec{E}^i &= E_0\left(\vec{a}_x\cos\theta_1 - \vec{a}_z\sin\theta_1\right) e^{-j\vec{k}_i\cdot\vec{r}}\\ \vec{E}^r &= \Gamma_1 E_0\left(\vec{a}_x\cos\theta_1 + \vec{a}_z\sin\theta_1\right) e^{-j\vec{k}_r\cdot\vec{r}}.\end{aligned} \tag{31}$$

At $z < 0$, the transmitted magnetic and electric fields are given by

$$\vec{H}^t = \frac{T_1 E_0}{\zeta_{\mathit{eff}}^{\mathrm{TM}}}\vec{a}_y e^{-j\vec{k}_t\cdot\vec{r}} \tag{32}$$

$$\vec{E}^t = T_1 E_0\left(\vec{a}_x\cos\theta_2 - \vec{a}_z\sin\theta_2\right) e^{-j\vec{k}_t\cdot\vec{r}}. \tag{33}$$

In Equations (30)–(33), the wavenumbers are given by

$$\begin{aligned}\vec{k}_i &= \left(\vec{a}_x\sin\theta_1 + \vec{a}_z\cos\theta_1\right) k_0\\ \vec{k}_r &= \left(\vec{a}_x\sin\theta_1 - \vec{a}_z\cos\theta_1\right) k_0\\ \vec{k}_t &= \left(\vec{a}_x\sin\theta_2 + \vec{a}_z\cos\theta_2\right) k_{\mathit{eff}}^{\mathrm{TM}}.\end{aligned} \tag{34}$$

The same procedure as used in the TE case allows us to represent the effective electric surface susceptibilities at the interfaces A and B:

$$\chi_{ES,A}^{xx} = \frac{\frac{1-\Gamma_1}{\zeta_0} - T\sqrt{\frac{\cos\theta_2}{\zeta_0\zeta_{\mathit{eff}}^{\mathrm{TM}}\cos\theta_1}}}{\frac{j\omega\varepsilon_0}{2}\left\{(1+\Gamma_1)\cos\theta_1 + T\sqrt{\frac{\zeta_{\mathit{eff}}^{\mathrm{TM}}\cos\theta_2}{\zeta_0\cos\theta_1}}\cos\theta_2\right\}} \tag{35}$$

$$\chi_{ES,B}^{xx}=\frac{\frac{1-\Gamma_2}{\zeta_{\mathit{eff}}^{\mathrm{TM}}}-T\sqrt{\frac{\cos\theta_1}{\zeta_0\zeta_{\mathit{eff}}^{\mathrm{TM}}\cos\theta_2}}}{\frac{j\omega\varepsilon_0}{2}\left\{(1+\Gamma_2)\cos\theta_2+T\sqrt{\frac{\zeta_0\cos\theta_1}{\zeta_{\mathit{eff}}^{\mathrm{TM}}\cos\theta_2}}\cos\theta_1\right\}}. \tag{36}$$

By letting $\chi_{ES,A}^{xx}=\chi_{ES,B}^{xx}$ in these equations, we can solve for the effective wave impedance of the metamaterial:

$$\zeta_{\mathit{eff}}^{\mathrm{TM}}=\sqrt{\frac{\mu_{r,\mathit{eff}}^{\mathrm{TM}}}{\varepsilon_{r,\mathit{eff}}^{\mathrm{TM}}}}\zeta_0=\frac{\left\{(1+\Gamma_1)\left(1-\Gamma_2\right)+T^2\right\}\cos\theta_1}{\left\{(1-\Gamma_1)\left(1+\Gamma_1\right)+T^2\right\}\cos\theta_2}\zeta_0. \tag{37}$$

Note that Equation (37) for the case of normal incidence ($\theta_1=\theta_2=0$) is reduced simply to Equation (11) in [35], as in the TE case.

We can also find the effective relative permittivity and permeability from Equations (10) and (37):

$$\varepsilon_{r,\mathit{eff}}^{\mathrm{TM}}=\pm\frac{\lambda_0\sqrt{\frac{1}{\lambda_c^2}-\left\{\frac{1}{2\pi(L2-L1)}\left[\ln\left\{\frac{S_{21}^{L2}\left(S_{11}^{L1}-\Gamma_1\right)}{S_{21}^{L1}\left(S_{11}^{L2}-\Gamma_1\right)}\right\}+j2\pi m\right]\right\}^2}}{\frac{\left\{(1+\Gamma_1)\left(1-\Gamma_2\right)+T^2\right\}\cos\theta_1}{\left\{(1-\Gamma_1)\left(1+\Gamma_1\right)+T^2\right\}\cos\theta_2}}, \tag{38}$$

$$\mu_{r,\mathit{eff}}^{TM}=\pm\lambda_0\sqrt{\frac{1}{\lambda_c^2}-\left\{\frac{1}{2\pi(L2-L1)}\left[\ln\left\{\frac{S_{21}^{L2}\left(S_{11}^{L1}-\Gamma_1\right)}{S_{21}^{L1}\left(S_{11}^{L2}-\Gamma_1\right)}\right\}+j2\pi m\right]\right\}^2}$$
$$\cdot\frac{\left\{(1+\Gamma_1)(1-\Gamma_2)+T^2\right\}\cos\theta_1}{\left\{(1-\Gamma_1)(1+\Gamma_1)+T^2\right\}\cos\theta_2}. \tag{39}$$

Again, it should be noticed that $|k_0 n_{\mathit{eff}} a|<1$ must be satisfied. Otherwise, the correctness of the effective material parameters computed from the equations in this paper cannot be guaranteed.

4. RESULTS AND DISCUSSION

4.1. An Array of Magneto-dielectric Cubes with $\varepsilon_r=\mu_r$

In this section, we discuss the effective material properties of magneto-dielectric cubes ($\varepsilon_r=\mu_r$) obtained from our equations for the TE and TM cases derived in the previous sections. An array of cubes has been studied and shown to demonstrate effective negative parameters in several papers [5, 44]. We can predict that the metamaterial composed of a cubic array of cubes has isotropic properties if the lattice constants in the x, y, and z directions are the same and are chosen so that $|k_0 n_{\mathit{eff}} a|<1$. This structure obeys $S_{11}=S_{22}$ and $S_{21}=S_{12}$, and

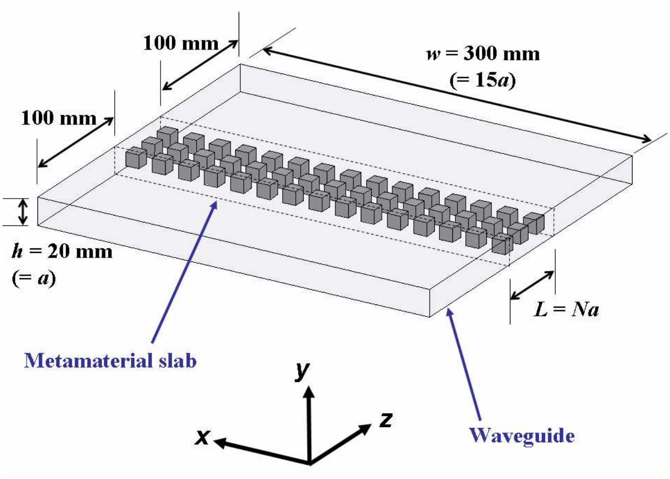

Figure 3. Illustration of an array of magneto-dielectric cubes placed in a waveguide for the full-wave simulation.

therefore the assumptions used to derive the equations in this paper are supported.

We first obtained numerical S-parameters from a 3-D full-wave simulation using the commercial software CST Microwave Studio†. Figure 3 shows the simulated structure used for the array of magneto-dielectric cubes. In Figure 3, the width and height of the waveguide lay in the x and y directions, and the input and output ports were assigned on the x-y planes. We chose the cubes to have permittivity and permeability of $\varepsilon_r = \mu_r = 40 - j0.004$ and a side length of 10 mm. The lattice constant of the metamaterial was $a = 20$ mm, and 15 cubes were repeated in the x direction to fill the waveguide of 300-mm width. We would have preferred to make the waveguide width as wide as possible, since the effective refractive index and the cutoff frequency of the loaded waveguide were not known at this stage. From this metamaterial configuration, an array of these magneto-dielectric cubes is predicted to resonate above the cutoff frequency of 0.5 GHz of the air-filled waveguide. The simulations were performed with different numbers of layers, $N1 = 2$ ($L1 = N1 \cdot a = 40$ mm) and $N2 = 3$ ($L2 = N2 \cdot a = 60$ mm), by replacing the waveguide walls by perfect electric conductor (PEC) and perfect magnetic conductor (PMC) boundaries for the TE and TM cases, respectively. The

---

† Reference to specific software is provided only for informational purposes and does not constitute any endorsement by the National Institute of Standards and Technology.

theoretical study in [45] has shown that boundary effects should not be very significant for a metamaterial of this type ($\varepsilon_r = \mu_r$), since the study predicted that the effective wave impedance is the same as that of air.

To compare our results with those extracted from a different method in the literature, we used the algorithm proposed by Menzel et al. [25]. They presented explicit expressions to extract the effective material properties of a metamaterial exposed to electromagnetic fields of the TE and TM polarizations by extending Smith's equations [21, 22] which are based on the Fresnel reflection coefficient such as the Nicolson-Ross-Wier (NRW) algorithm [46–48]. Menzel's method requires knowledge of the S-parameters only for a single slab length. Similarly to the original work of Smith's group, the effective properties extraction technique of Menzel et al. does not account for the boundary effects on the determination of the material parameters. For the comparisons in this paper, we used the S-parameters for $L2$ (3-layer)-thick metamaterial slab when using Menzel's equations.

The real and imaginary parts of the refractive index calculated from Equation (10) and Menzel's equation are plotted in Figures 4(a) and (b). In the real and imaginary parts, apart from the resonance at 0.880 GHz and the negative slope in real part around 0.865–0.870 GHz, our Equation (10) and Menzel's equation give refractive indices that are in good agreement. In addition, we see from Figure 4(a) that our present method and Menzel's method show negative values for the real part of the refractive index around the resonance 0.866–0.877 GHz and

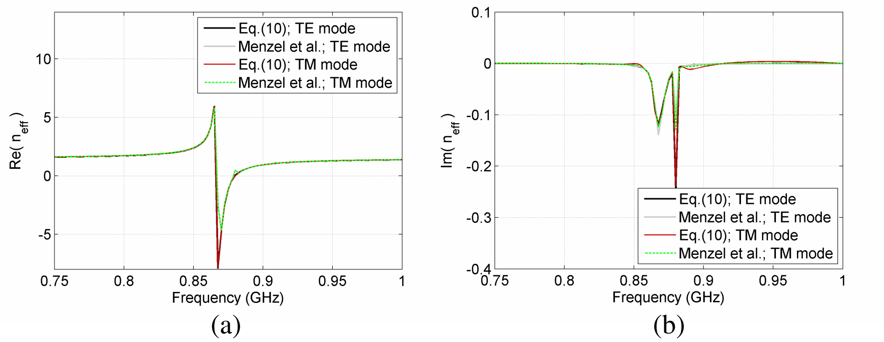

(a) (b)

Figure 4. Comparison of the real and imaginary parts of the effective refractive index of the array of magneto-dielectric cubes ($\varepsilon_r = \mu_r$) extracted with Equation (10) (TE and TM) and Menzel's equation. (a) Real part of refractive index. (b) Imaginary part of refractive index.

from Figure 4(b) that $\mathrm{Im}\,(n_{\mathit{eff}}) \leq 0$ over the entire frequency range, since the magneto-dielectric cubes employed to make this array are passive particles. The effective refractive indices from the TE and TM polarizations are shown to be identical, and we therefore can confirm that this metamaterial composed of inclusions having $\varepsilon_r = \mu_r$ is isotropic.

Cutoff frequencies for each propagation mode in a medium placed in the waveguide are found from f_c/n_{eff}. Figure 5 shows possible propagation modes inside the metamaterial slab region in the waveguide. Notice that no propagation modes (even TE_{10} mode) exist at 0.866, 0.878–0.888 GHz and 0.866, 0.875–0.888 GHz, respectively, from our and Menzel's equations, due to very small refractive index. Thus, as the frequency increases, a mode can begin to propagate, then to be cutoff, and then propagate again. Furthermore, Figure 5 indicates that, except near 0.866 GHz, at least 3 modes, TE_{10}, TE_{20} and TE_{30}, may propagate at 0.822–0.873 GHz (as our result shows) or 0.820–0.870 GHz (as Menzel's method shows) because the effective refractive index becomes very large at those frequencies. Lowering the cutoff frequencies may allow higher-order modes generated by each cube to propagate within the metamaterial slab. If the dominant-mode incident wave from the input port is coupled to the higher-order modes and the higher-order modes that are recoupled to the dominant mode are detected at the input and output ports, the accuracy of

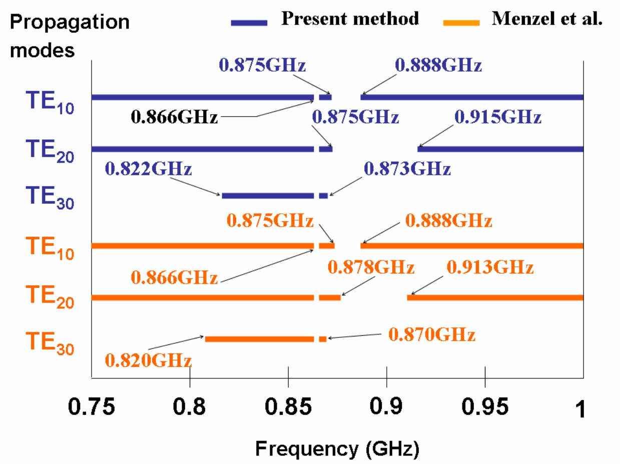

Figure 5. Propagation modes inside the slab of the array of magneto-dielectric cubes ($\varepsilon_r = \mu_r$) placed in the waveguide, and cutoff frequency computed from f_c/n_{eff} with our and Menzel's equations for n_{eff}.

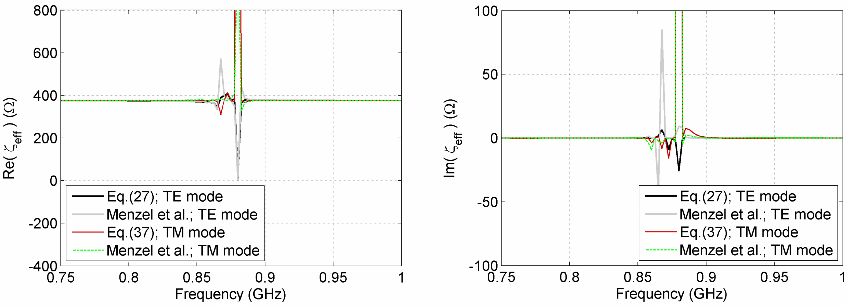

(a) (b)

Figure 6. Comparison of the real and imaginary parts of the effective wave impedance of the array of magneto-dielectric cubes ($\varepsilon_r = \mu_r$) extracted with Equations (27) (TE) and (37) (TM) and Menzel's equation. (a) Real part of wave impedance. (b) Imaginary part of wave impedance.

the extracted material parameters calculated by our and Menzel's techniques may be degraded.

The real and imaginary parts of the effective wave impedance of the metamaterial from Equations (27) (TE propagation) and (37) (TM) and from Menzel's equations are shown in Figures 6(a) and (b). Comparison between the results from these two algorithms for both TE and TM modes for this paper and Menzel's work agree as a whole in the real and imaginary values. At frequencies before and after the resonance, the real part is shown to be 375 Ω and 377 Ω, approximately the wave impedance of air. In spite of the fact that no mode propagates at the resonance, as mentioned above, around the resonance the effective wave impedance $\mathrm{Re}(\zeta_{eff}) = 385\,\Omega$ and $\mathrm{Im}(\zeta_{eff}) = 0\,\Omega$. This is expected because the permittivity and permeability of the particles have the same value, so that $\zeta_{eff} \cong \zeta_0$ would be predicted.

Figures 7 and 8 show the real and imaginary permittivity and permeability found from the equations presented in this paper and from the method of Menzel's paper. The permittivity and permeability demonstrate almost identical material parameter values and resonance frequency. The real part of the permittivity calculated for the TE polarization provides a narrow spike at 0.880 GHz, while the permittivity for the TM polarization does not. The real part of the permeability in the TM case has a spike at the same frequency, whereas the one in TE does not. We deduce that, although the values of ε_r and μ_r of the magneto-dielectric cubic particles are the same, spatial dispersions happen, and the effective permittivity $\varepsilon_{r,eff}$

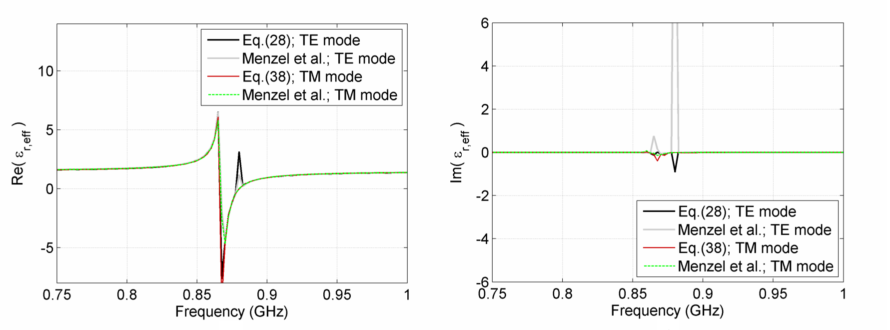

(a) (b)

Figure 7. Comparison of the real and imaginary parts of the effective permittivity of the array of magneto-dielectric cubes ($\varepsilon_r = \mu_r$) extracted with Equations (28) (TE) and (38) (TM) and Menzel's equation. (a) Real part of permittivity. (b) Imaginary part of permittivity.

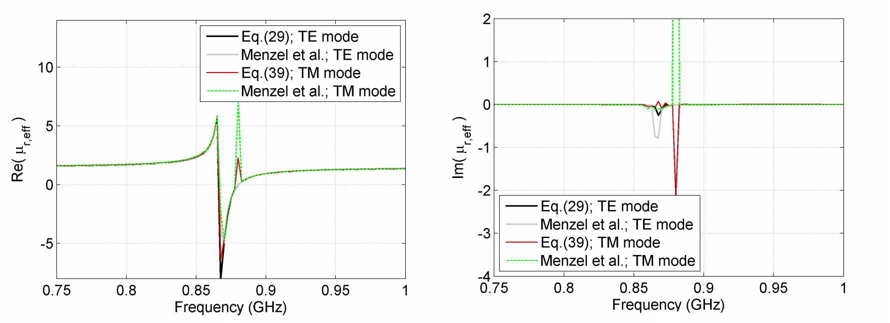

(a) (b)

Figure 8. Comparison of the real and imaginary parts of the effective permeability of the array of magneto-dielectric cubes ($\varepsilon_r = \mu_r$) extracted with Equations (29) (TE) and (39) (TM) and Menzel's equation. (a) Real part of permeability. (b) Imaginary part of permeability.

and permeability $\mu_{r,eff}$ may have different values because a wave traveling within the waveguide propagates at different propagation angles, depending on frequencies. We also see that, at that frequency, a positive divergence occurs in the imaginary part computed with Menzel's algorithm.

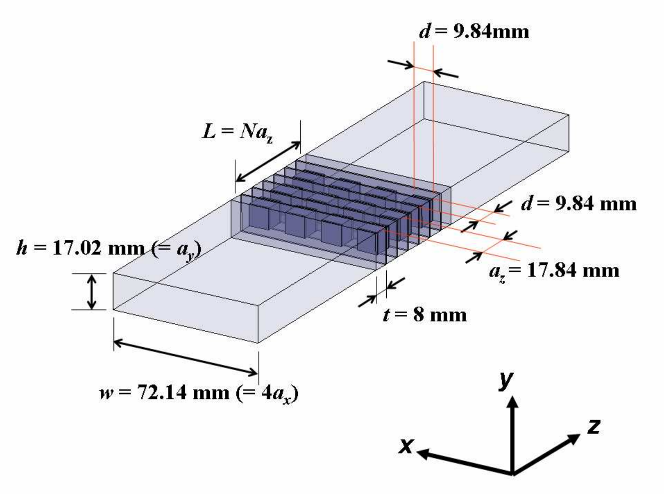

Figure 9. Illustration of an array of dielectric ($\mathrm{TiO_2}$) cubes placed in a waveguide for the full-wave simulation.

4.2. An Array of Dielectric ($\mathrm{TiO_2}$) Cubes

In this section, we discuss the effective material properties of an array of dielectric cubes (with $\varepsilon_r \neq \mu_r$) obtained from our present equations for the TE and TM polarizations. Similarly to the previous section, it is predicted that the metamaterial of a cubic array of cubes has isotropic properties if the lattice constants are chosen to be the same in the x, y, and z directions. In the case of this section, due to $\varepsilon_r \neq \mu_r$, the effective properties are expected to exhibit stopband characteristics around the resonances, which results from a wave impedance very different from that of air.

We attempted to obtain S-parameters from a 3-D full-wave simulation using CST Microwave Studio[‡]. Figure 9 illustrates the structure for an array of dielectric cubes placed in the waveguide. For the dielectric cubes, we used a $\mathrm{TiO_2}$ material whose permittivity and permeability are $\varepsilon_r = 108.2 - j0.053$ and $\mu_r = 1$. The side length of cubes was $d = 9.84\,\mathrm{mm}$ and we chose the lattice constants $a_x = 18.035\,\mathrm{mm}$, $a_y = 17.020\,\mathrm{mm}$, and $a_z = 17.840\,\mathrm{mm}$ respectively in the x, y, and z directions. These lattice constants a_x, a_y, and a_z are not identical in this metamaterial configuration because of the limitations on dimensions of the dielectric cubes and the waveguide,

---

[‡] Reference to specific software is provided only for informational purposes and does not constitute any endorsement by the National Institute of Standards and Technology.

and the dimensions need to have an integer number of lattice constants for the waveguide wall dimensions. However, we can expect these lattice constants to provide "almost" isotropic material properties of the metamaterial at the frequencies for $|k_0 n_{eff} a| < 1$ and away from a resonance of the metamaterial, where $n_{eff} \cong 0$. In Figure 9, the dielectric cubes were embedded in 8-mm-thick foamed-polystyrene sheets ($\varepsilon_r \cong 1.03$), and one-layer metamaterial sheets and foamed-polystyrene sheets were alternated in the z direction (propagation direction) to hold the dielectric constituents for the measurement configuration. In the simulation, the height of the waveguide was $h = 17.02\,\text{mm}$; that is one half of that of a WR-284 (S band) waveguide, to save computer resources and simulation time. The width was $w = 72.14\,\text{mm}$; that is the same as that of a WR-284 waveguide. We simulated the metamaterial slab of 2 and 3 layers that give the slab lengths, $L1 = 35.68\,\text{mm}$ and $L2 = 53.52\,\text{mm}$. The PEC boundary conditions were assigned for the waveguide walls for the TE case. The waveguide walls were replaced by the PMC boundary conditions for the TM case. We performed the simulations at 2.2–4.0 GHz on $L1$ and $L2$ for the TE and TM polarizations.

Furthermore, we experimentally constructed an array of these dielectric cubes, by use of the dimensions used for the simulations, to measure the S-parameters. In our experiment, we employed the WR-284 waveguide instead of the low-profile simulated waveguide. We measured the S-parameters in the same frequency range as used for the simulations. The metafilm (one-layer metamaterial) used to create the

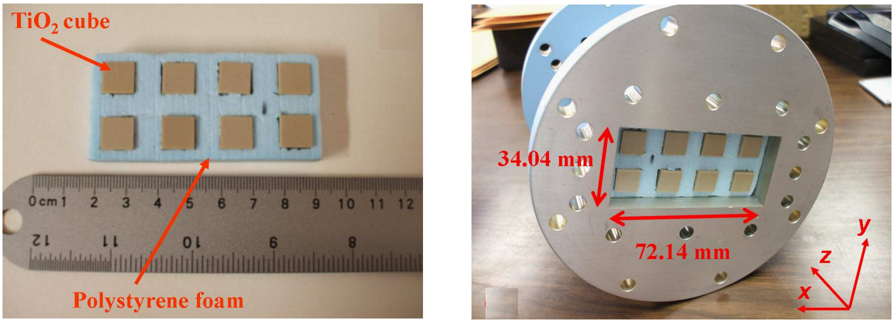

(a) (b)

Figure 10. (a) Metafilm (one-layer metamaterial composed of dielectric cubes (TiO_2)) used to fabricate a metamaterial slab. (b) WR-284 waveguide loaded with the metamaterial slab sample for the measurement.

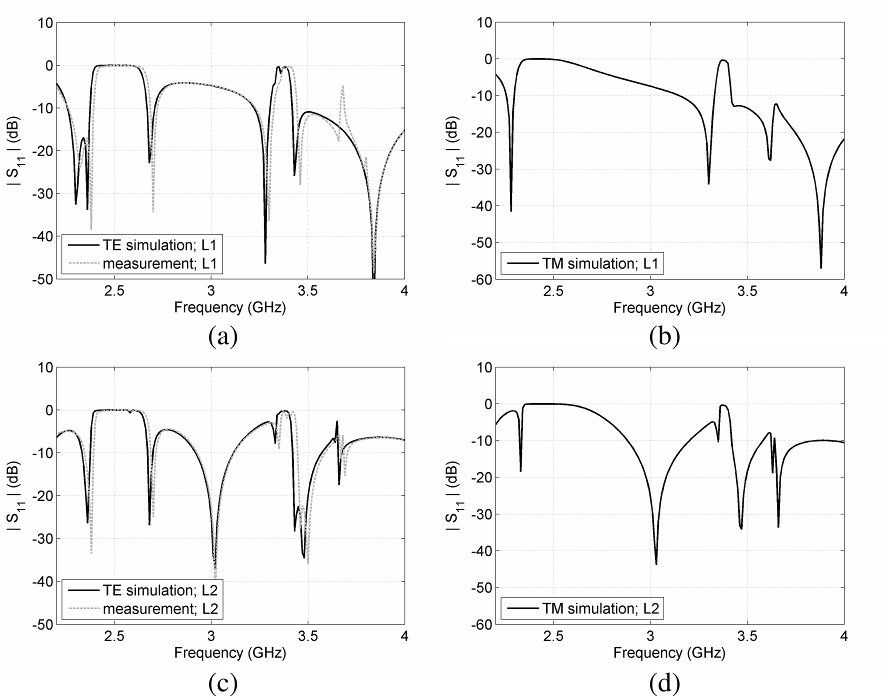

Figure 11. Reflection (S_{11}) simulated and measured for the metamaterial slab samples composed of the array of dielectric (TiO_2) cubes. (a) S_{11} from the TE simulation and measurement on $L1$ (2 layers). (b) S_{11} from the TM simulation on $L1$ (2 layers). (c) S_{11} from the TE simulation and measurement on $L2$ (3 layers). (d) S_{11} from the TM simulation on $L2$ (3 layers).

metamaterial slab is shown in Figure 10(a). The other metafilm sheets were inserted into the waveguide behind it to make up the metamaterial slab in the waveguide. The metamaterial in Figure 10(b) is expected to exhibit the same effective material properties as the metamaterial in Figure 9.

Figure 11 shows S_{11} for the sample lengths $L1$ and $L2$ from CST Microwave Studio[§] simulations in the TE and TM cases and from the measurement with the waveguide, while Figure 12 presents S_{21}. Very good agreements between the simulated and measured data are confirmed in Figures 11 and 12. Very slight discrepancies are presumed

---

[§] Reference to specific software is provided only for informational purposes and does not constitute any endorsement by the National Institute of Standards and Technology.

to result from the manufacturing errors on the dimensions and the permittivity of the dielectric cubes and due to errors on the alignments of the cubes and imperfections in the holes cut in the foamed-polystyrene plate for the measurement. The uncertainties of these types of S-parameter measurements are discussed and summarized in [49]. As predicted, stopbands are observed around the resonance frequencies of 2.39–2.65 GHz and 3.33–3.43 GHz, where S_{11} for $L1$ and $L2$ are very large and S_{21} very small, since the values ε_r and μ_r of the cubes are different. Comparison between S_{21} data for $L1$ and $L2$ in the TE and TM cases shows that the metamaterial slab exhibits more lossy characteristics around the resonances as the slab lengths become larger. These resonances shift towards higher frequencies with decreasing side length of the cubes, as particles become smaller. If

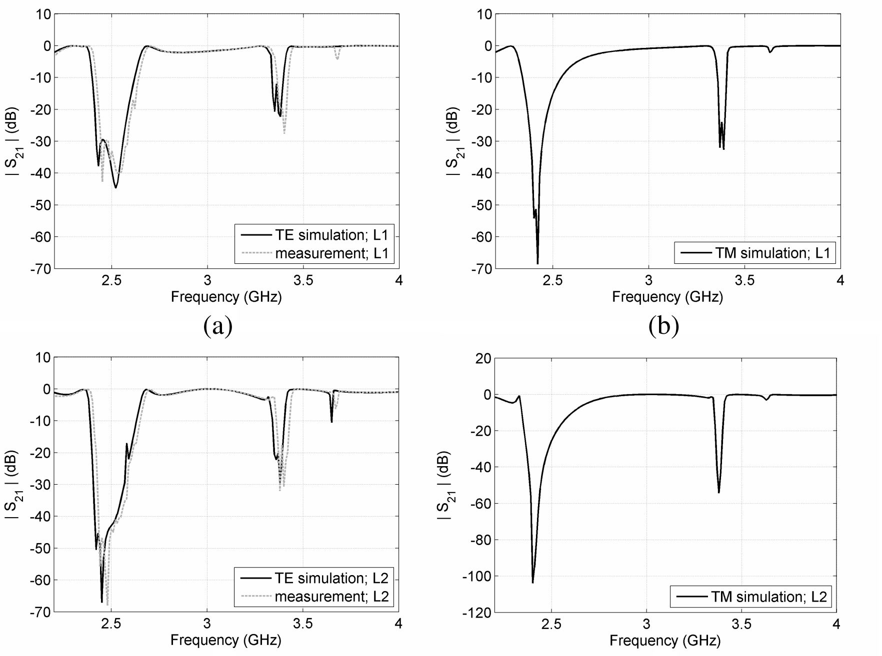

(a) (b)

(c) (d)

Figure 12. Transmission (S_{21}) simulated and measured for the metamaterial slab samples composed of the array of dielectric (TiO_2) cubes. (a) S_{21} from the TE simulation and measurement on $L1$ (2 layers). (b) S_{21} from the TM simulation on $L1$ (2 layers). (c) S_{21} from the TE simulation and measurement on $L2$ (3 layers). (d) S_{21} from the TM simulation on $L2$ (3 layers).

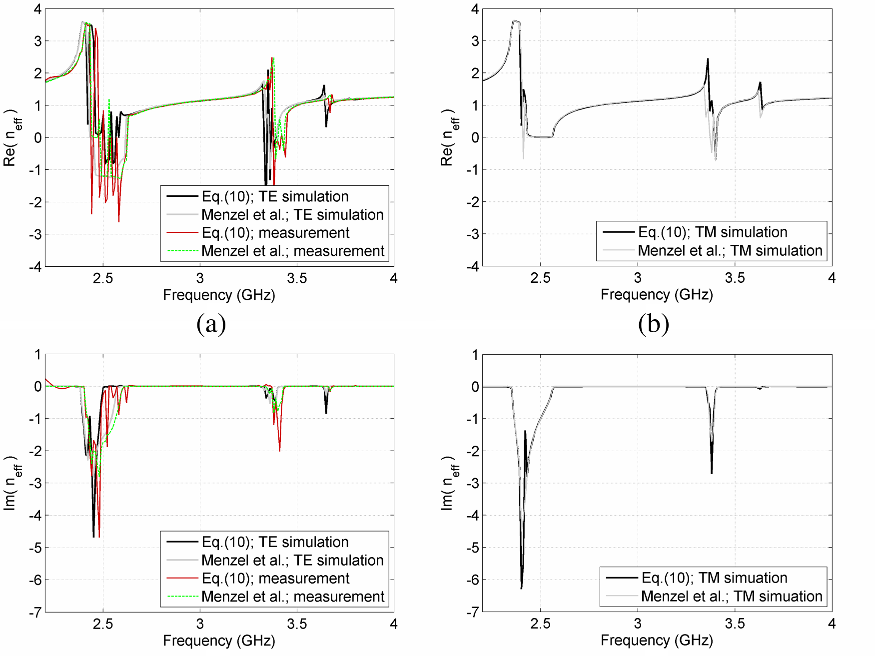

(a) (b)

(c) (d)

Figure 13. Comparison of the real and imaginary parts of the effective refractive index of the array of dielectric ($\mathrm{TiO_2}$) cubes extracted with Equation (10) (TE, measurement and TM) and Menzel's equation. (a) Real part of refractive index from the TE simulation and measurement. (b) Real part of refractive index from the TM simulation. (c) Imaginary part of refractive index from the TE simulation and measurement. (d) Imaginary part of refractive index from the TM simulation.

larger permittivity of the cubes is chosen, more resonances occur in the frequency range illustrated in Figures 11 and 12.

Figures 13(a) and (b) show the real part of the effective refractive index extracted from the metamaterial slab simulated as depicted in Figure 9 and measured as in Figure 10(b) with Equation (10). In Figure 13(a), the resonances are confirmed roughly around 2.40–2.62 GHz, 3.34–3.45 GHz, and 3.64–3.69 GHz. The configuration of the metamaterial formed of cubes with $\varepsilon_r \neq \mu_r$ is not expected to provide a negative refractive index. In Figure 13(a), the refractive index from the TE simulation and measurement is seen to be very noisy at the resonances, and the negative values are thought to be due only to experimental or numerical errors in the S-parameter data. S_{21} is very small in these ranges. The results of the real part of the effective refractive index from Equation (10) and Menzel's equation with the measured S-parameters show overall agreement outside the resonances. In Figure 13(a), the refractive index obtained from the measured data shifts towards higher frequencies compared to those from the simulated data; the shifted S-parameters seen in Figures 11 and 12 can explain this. Figure 13(b) shows the real part of the refractive index obtained from the simulation in the TM case that virtually agrees with that from the TE simulation case in Figure 13(a). This indicates that the metamaterial we simulated and measured

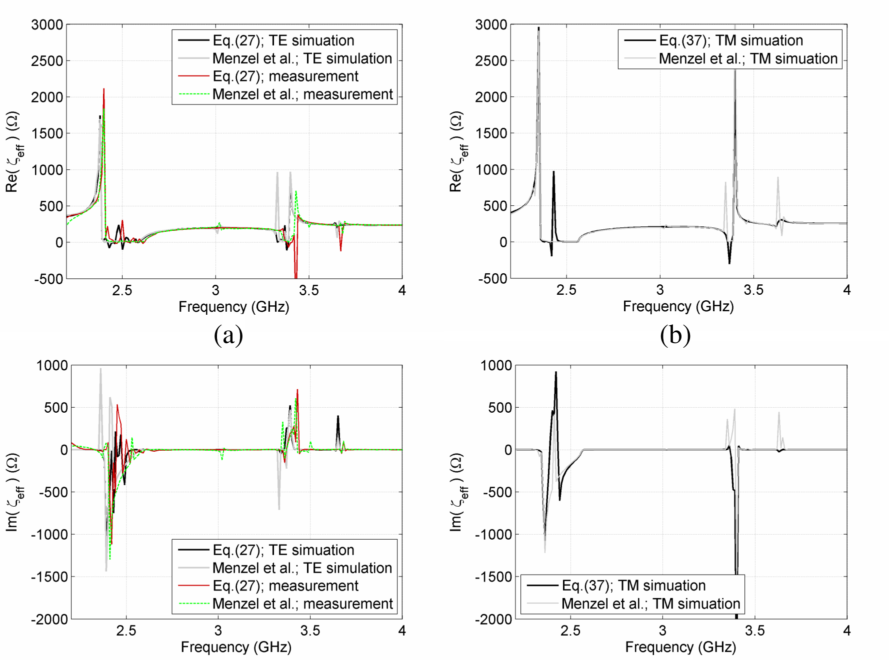

(a) (b)

(c) (d)

Figure 14. Comparison of the real and imaginary parts of the effective wave impedance of the array of dielectric (TiO_2) cubes extracted with Equations (27) (TE and measurement) and (37) (TM) and Menzel's equation. (a) Real part of wave impedance from the TE simulation and measurement. (b) Real part of wave impedance from the TM simulation. (c) Imaginary part of wave impedance from the TE simulation and measurement. (d) Imaginary part of wave impedance from the TM simulation.

exhibits an approximately isotropic refractive index. We can predict that if a completely cubic array of cubes is implemented, perfectly isotropic effective material parameters would be realized. A stopband is observed at 2.44–2.56 GHz. We can also see from Figure 13(b) that, around the resonance frequencies, the refractive index in the TM incidence shows discrepancies between the positive peak values that Equation (10) and Menzel's equation yield. The refractive index calculated from Equation (10) attains peaks of 2.45–1.72, respectively, at 3.36 GHz and 3.63 GHz and from Menzel's equation its peaks of 1.63 and 1.46, respectively, at 3.34 GHz and 3.62 GHz. Better agreement between Equation (10) and Menzel's equation is observed for the TM case than for the TE case. This appears to mean that in this example, boundary effects are less important for the TM case than for the TE case.

In Figures 13(c) and (d), we present the imaginary part of the refractive index extracted from Equation (10) and Menzel's equations with the TE and TM simulated and measured S-parameter data. The results from the TE simulated and measured data are shown to be oscillatory around the resonances and yet have physical values that obey $\mathrm{Im}\,(n_{\mathit{eff}}) \leq 0$ over all frequencies. In the TM case, plotted in Figure 13(d), the imaginary parts found from Equation (10) and Menzel's equation show overall agreement.

Figures 14(a) and (b) show the real part of the wave impedance from Equations (27), (37) and Menzel's method for the simulations and measurement. Resonances are seen at 2.38–2.62, 3.34–3.44, and 3.64–3.69 GHz that are entirely in agreement with the resonance frequencies of the refractive index. However, we see that Menzel's algorithm gives sharp peaks at 3.33 GHz in the TE case and at 3.35 GHz and 3.63 GHz in the TM case, whereas our method shows no peaks at these frequencies. The discrepancies can be explained by the fact that our equations for the wave impedance are derived by use of the GSTCs that account for boundary effects. Furthermore, the spike in Menzel's result at 3.01–3.02 GHz may be due to the metamaterial length, since these frequencies seem to correspond to an integer multiple of the length (see the very small S_{11} in Figure 11(a)). As was seen in the plots of the refractive index, the wave impedance that results from the measurement is moved to higher frequencies, compared with that from the simulation in the TE case. Figures 14(a) and (b) demonstrate that $\mathrm{Re}(\zeta_{\mathit{eff}}) \geq 0$ meaning the physical requirement for the metamaterial composed of passive components, although some negative spikes due to noise are seen from our results.

Finally, the real parts of the effective permittivity and permeability are shown in Figures 15 and 16. We see that a negative

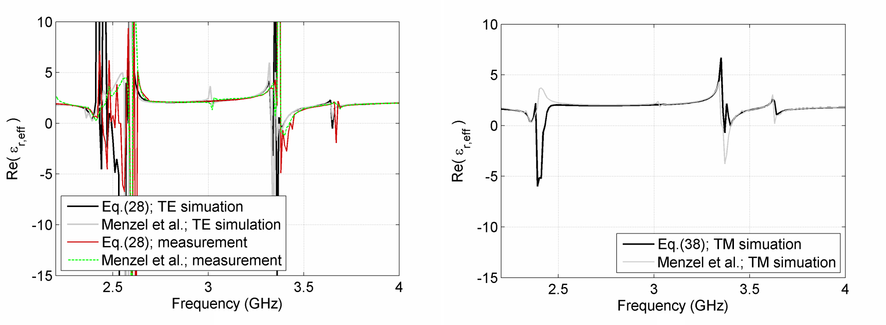

(a) (b)

Figure 15. Comparison of the real part of the effective permittivity of the array of dielectric (TiO_2) cubes extracted with Equations (28) (TE and measurement) and (38) (TM) and Menzel's equation. (a) Real part of permittivity from the TE simulation and measurement. (b) Real part of permittivity from the TM simulation.

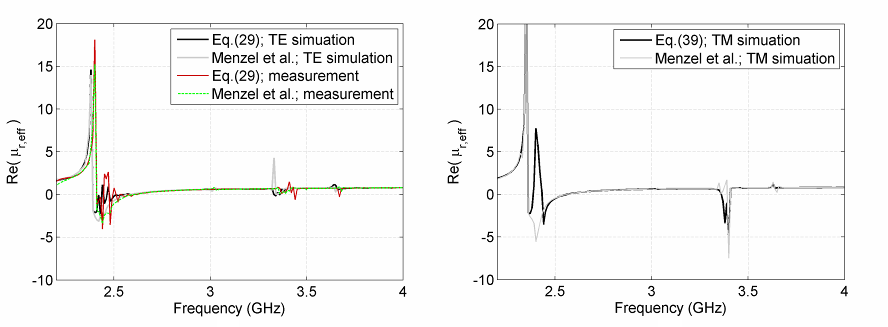

(a) (b)

Figure 16. Comparison of the real part of the effective permeability of the array of dielectric (TiO_2) cubes extracted with Equations (29) (TE and measurement) and (39) (TM) and Menzel's equation. (a) Real part of permeability from the TE simulation and measurement. (b) Real part of permeability from the TM simulation.

permittivity happens only around 3.36–3.40 GHz and a negative permeability only around 2.36–2.56 GHz. We can deduce that the anomalous permittivity and permeability are due to the stopband properties, where S_{21} is very small and $\mathrm{Re}(\zeta_{eff}) \cong 0$. Similarly to the wave impedances retrieved from our and Menzel's equations, we observe that our and Menzel's results have very different peaks.

5. CONCLUSION

We have presented the equations to extract the effective refractive index of a metamaterial based on either measured or simulated S-parameters for two different sample lengths, and then derived the equations for the effective wave impedance with the GSTCs to account for boundary effects in TE and TM incidence cases. The effective permittivity and permeability have been calculated from the refractive index and wave impedance. The algorithm presented in this paper facilitates the material parameter retrieval of a metamaterial sample placed in a waveguide applicable for more realistic measurements than that in free space.

We have attempted to extract the effective material properties of a cubic array of magneto-dielectric cubes having $\varepsilon_r = \mu_r$ placed in a waveguide supporting a TE or TM wave by use of simulated S-parameters. In this metamaterial case, our results show good agreement with those from Menzel's (NRW-type) method that does not properly account for boundary effects. A resonance is observed at 0.866–0.877 GHz, near which negative refractive index, permittivity, and permeability are confirmed. The effective refractive index of the metamaterial exhibits perfect isotropic behavior. The wave impedance is the same as that of air as a whole. Although the lattice constants in the x, y, and z directions are the same in this metamaterial configuration, the effective permeability and permeability do not necessarily show the same values near resonance, 0.880 GHz. This is interpreted as the spatial dispersion phenomenon that is attributed to a wave propagating at different incidence angles depending on frequencies. We have also shown that when a metamaterial is inserted into a waveguide, cutoff frequency bands exist even in the TE_{10} mode due to very small refractive index and that the cutoff frequencies for higher-order modes are lowered and able to propagate within the metamaterial due to large refractive index. Perhaps, this may deteriorate the accuracies of the material parameters determined from our and Menzel's algorithms in this measurement.

We have also examined another case when dielectric (TiO_2) cubes are arranged in a waveguide. For the dielectric cubes, we have simulated S-parameters in the TE and TM cases and conducted S-parameter measurements for the loaded waveguide. Although the lattice constants a_x, a_y, and a_z are not exactly the same, due to the limitations of the dimensions of the cubes and waveguide, the effective material properties are shown to be "almost" isotropic. In terms of the retrieved wave impedance, permittivity, and permeability, our equations that account for boundary effects show some discrepancies around the resonances when compared to Menzel's equations that do not. Moreover, Menzel's method shows peaks at the frequency that may correspond to an integer multiple of the length of the metamaterial slab, whereas our present method does not.

ACKNOWLEDGMENT

The authors are deeply indebt to the special technical support arrangement by Dr. M. D. Janezic and Ms. C. A. Hammerschmidt at the National Institute of Standards and Technology (NIST) in Boulder. This research was supported in part by a grant from Sandia National Laboratories.

REFERENCES

1. Pendry, J. B., A. J. Holden, D. J. Robbins, and W. J. Stewart, "Low frequency plasmons in thin-wire structures," *J. Phys. Cond. Mat.*, Vol. 10, 4785–4809, 1998.
2. Pendry, J. B., A. J. Holden, D. J. Robbins, and W. J. Stewart, "Magnetism from conductors and enhanced nonlinear phenomena," *IEEE Trans. Microw. Theory Tech.*, Vol. 47, No. 11, 2075–2084, 1999.
3. Saadoun, M. M. I. and N. Engheta, "A reciprocal phase shifter using novel pseudochiral or Omega medium," *Microwave Opt. Tech. Lett.*, Vol. 5, No. 4, 184–188, 1992.
4. Lindell, I. V., A. H. Sihvola, S. A. Tretyakov, and A. J. Viitanen, *Electromagnetic Waves in Chiral and Bi-isotropic Media*, Artech House, Boston, 1994.
5. Holloway, C. L., E. F. Kuester, J. Baker-Jarvis, and P. Kabos, "A double negative (DNG) composite medium composed of magnetodielectric spherical particles embedded in a matrix," *IEEE Trans. Antennas Propag.*, Vol. 51, No. 10, 2596–2603, 2003.
6. Kim, J. and A. Gopinath, "Simulation of a metamaterial containing cubic high dielectric resonators," *Phys. Rev. B*, Vol. 76, 115126, 2007.
7. Zhao, Q., L. Kang, B. Du, H. Zhao, Q. Xie, X. Huang, B. Li, J. Zhou, and L. Li, "Experimental demonstration of isotropic negative permeability in a three-dimensional dielectric composite," *Phys. Rev. Lett.*, Vol. 101, 027402, 2008.
8. Wang, J., S. Qu, H. Ma, Y. Yang, X. Wu, Z. Xu, and M. Hao, "Wide-angle polarization-independent planar left-handed

metamaterials based on dielectric resonators," *Progress In Electromagnetics Research B*, Vol. 12, 243–258, 2009.

9. Pendry, J. B., "Negative refraction makes a perfect lens," *Phys. Rev. Lett.*, Vol. 85, 3966–3969, 2000.
10. Grbic, A. and G. V. Eleftheriades, "Overcoming the diffraction limit with a planar left-handed transmission-line lens," *Phys. Rev. Lett.*, Vol. 92, 117403, 2004.
11. Yang, F. and Y. Rahmat-Samii, *Electromagnetic Band Gap Structures in Antenna Engineering*, Cambridge University Press, New York, 2009.
12. Landy, N. I., S. Sajuyigbe, J. J. Mock, D. R. Smith, and W. J. Padilla, "Perfect metamaterial absorber," *Phys. Rev. Lett.*, Vol. 100, 207402, 2008.
13. Li, Y., Y. Xie, H. Zhang, Y. Liu, Q. Wen, and W. Ling, "The strong non-reciprocity of metamaterial absorber: Characteristic, interpretation and modeling," *J. Phys. D. Appl. Phys.*, Vol. 42, 095408, 2009.
14. Wang, J., S. Qu, Z. Fu, H. Ma, Y. Yang, X. Wu, Z. Xu, and M. Hao, "Three-dimensional metamaterial microwave absorbers composed of coplanar magnetic and electric resonators," *Progress In Electromagnetics Research Letters*, Vol. 7, 15–24, 2009.
15. Engheta, N., "An idea for thin subwavelength cavity resonators using metamaterials with negative permittivity and permeability," *IEEE Antennas Wireless Propag. Lett.*, Vol. 1, 10–13, 2002.
16. Ozgun, O. and M. Kuzuoglu, "Utilization of anisotropic metamaterial layers in waveguide miniaturization and transitions," *IEEE Microw. Wireless Compon. Lett.*, Vol. 17, No. 11, 754–756, 2007.
17. Meng, F. Y., Q. Wu, and J. H. Fu, "Miniaturized rectangular cavity resonator based on anisotropic metamaterials bilayer," *Microwave Opt. Tech. Lett.*, Vol. 50, No. 8, 2016–2020, 2008.
18. Holloway, C. L., D. C. Love, E. F. Kuester, A. Salandrino, and N. Engheta, "Sub-wavelength resonators: On the use of metafilms to overcome the lambda/2 size limit," *IET Microw. Antennas Propag.*, Vol. 2, No. 2, 120–129, 2008.
19. Alù, A., F. Bilotti, N. Engheta, and L. Vegni, "Subwavelength, compact, resonant patch antennas loaded with metamaterials," *IEEE Trans. Antennas Propag.*, Vol. 55, No. 1, 13–25, 2007.
20. Bilotti, F., A. Alù, and L. Vegni, "Design of miniaturized metamaterial patch antennas with mu-negative loading," *IEEE Trans. Antennas Propag.*, Vol. 56, No. 6, 1640–1647, 2008.

21. Smith, D. R. and S. Schultz, "Determination of effective permittivity and permeability of metamaterials from reflection and transmission coefficients," *Phys. Rev. B*, Vol. 65, 195104, 2002.
22. Smith, D. R., D. C. Vier, T. Koschny, and C. M. Soukoulis, "Electromagnetic parameter retrieval from inhomogeneous metamaterials," *Phys. Rev. E*, Vol. 71, 036617, 2005.
23. Chen, H., J. Zhang, Y. Bai, Y. Luo, L. Ran, Q. Jiang, and J. A. Kong, "Experimental retrieval of the effective parameters of metamaterials based on a waveguide method," *Optics Express*, Vol. 14, No. 26, 12944–12949, 2006.
24. Carbonell, J., L. J. Roglá, V. E. Boria, and D. Lippens, "Design and experimental verification of backward-wave propagation in periodic waveguide structures," *IEEE Trans. Microw. Theory Tech.*, Vol. 54, No. 4, 1527–1533, 2006.
25. Menzel, C., C. Rockstuhl, T. Paul, and F. Lederer, "Retrieving effective parameters for metamaterials at oblique incidence," *Phys. Rev. B*, Vol. 77, 195328, 2008.
26. Cohn, S. B., "Microwave measurements on metallic delay media," *Proc. IRE*, Vol. 41, 1177–1183, 1953.
27. Brown, J. and W. Jackson, "The properties of artificial dielectrics at centimetre wavelengths," *Proc. IEE*, Vol. 102B, 11–16, London, 1955.
28. Scher, A. D. and E. F. Kuester, "Extracting the bulk effective parameters of a metamaterial via the scattering from a single planar array of particles," *Metamaterials*, Vol. 3, No. 1, 44–55, 2009.
29. Pekar, S. I., "The theory of electromagnetic waves in a crystal in which excitations are produced," *Sov. Phys. JETP*, Vol. 6, 785–796, 1958.
30. Silveirinha, M. G., C. A. Fernandes, and J. R. Costa, "Additional boundary conditions for a wire medium connected to a metallic surface," *New J. Phys.*, Vol. 10, 053011, 2008.
31. Silveirinha, M. G., "Additional boundary conditions for nonconnected wire media," *New J. Phys.*, Vol. 11, 113016, 2009.
32. Simovski, C. R. and S. A. Tretyakov, "Local constitutive parameters of metamaterials from an effective-medium perspective," *Phys. Rev. B*, Vol. 75, 195111, 2007.
33. Simovski, C. R., "Material parameters of metamaterials (a review)," *Opt. Spectr.*, Vol. 107, No. 5, 766–793, 2009.

34. Vinogradov, A. P., A. I. Ignatov, A. M. Merzlikin, S. A. Tretyakov, and C. R. Simovski, "Additional effective medium parameters for composite materials (excess surface currents)," *Opt. Express*, Vol. 19, No. 7, 6699–6704, 2011.
35. Kim, S., E. F. Kuester, C. L. Holloway, A. D. Aaron, and J. Baker-Jarvis, "Boundary effects on the determination of metamaterial parameters from normal incidence reflection and transmission measurements," *IEEE Trans. Antennas Propag.*, Vol. 59, No. 6, 2226–2240, 2011.
36. Marks, R. B. and D. F. Williams, "A general waveguide circuit theory," *J. Res. Nat. Inst. Stand. Technol.*, Vol. 97, No. 5, 553–562, 1992.
37. Huynen, I., C. Steukers, and F. Duhamel, "A wideband line-line dielectric method for liquids, soils, and planar substrates," *IEEE Trans. Instrum. Meas.*, Vol. 50, No. 5, 1343–1348, 2001.
38. Carchon, G. and B. Nauwelaers, "Accurate transmission line characterisation on high and low-resistivity substrates," *Proc. IEE Microw. Antennas Propag.*, Vol. 148, No. 5, 285–290, 2001.
39. Narita, K. and T. Kushta, "An accurate experimental method for characterizing transmission lines embedded in multilayer printed circuit boards," *IEEE Trans. Adv. Packag.*, Vol. 29, No. 1, 114–121, 2006.
40. Kuester, E. F., M. A. Mohamed, M. Picket-May, and C. L. Holloway, "Averaged transition conditions for electromagnetic fields at a metafilm," *IEEE Trans. Antennas Propag.*, Vol. 51, No. 10, 2641–2651, 2003.
41. Scher, A. D. and E. F. Kuester, "Boundary effects in the electromagnetic response of a metamaterial in the case of normal incidences," *Progress In Electromagnetics Research B*, Vol. 14, 341–381, 2009.
42. Vernon, R. J. and S. R. Seshadri, "Reflection coefficient and reflected power on a lossy transmission line," *Proc. IEEE*, Vol. 57, 101–102, 1969.
43. Mohamed, M. A., E. F. Kuester, M. Piket-May, and C. L. Holloway, "The field of an electric dipole and the polarizability of a conducting object embedded in the interface between dielectric materials," *Progress In Electromagnetics Research B*, Vol. 16, 1–20, 2009.
44. Holloway, C. L., M. A. Mohamed, E. F. Kuester, and A. Dienstfrey, "Reflection and transmission properties of a metafilm: With an application to a controllable surface composed of resonant particles," *IEEE Trans. Electromag. Compat.*, Vol. 47,

No. 4, 853–865, 2005.

45. Scher, A. D., “Boundary effects in the electromagnetic response of a metamaterial using the point-dipole interaction model,” Ph.D. Thesis, University of Colorado at Boulder, 2008.
46. Nicolson, A. M. and G. F. Ross, “Measurement of the intrinsic properties of materials by time-domain techniques,” *IEEE Trans. Instrum. Meas.*, Vol. 19, No. 4, 377–382, 1970.
47. Wier, W. B., “Automatic measurement of complex dielectric constant and permeability at microwave frequencies,” *Proc. IEEE*, Vol. 62, No. 1, 33–36, 1974.
48. Baker-Jarvis, J., E. J. Vanzura, and W. A. Kissick, “Improved technique for determining complex permittivity with transmission/reflection method,” *IEEE Trans. Microw. Theory Tech.*, Vol. 38, No. 8 1096–1103, 1990.
49. Baker-Jarvis, J., M. D. Janezic, J. H. Grosvenor, Jr., and R. G. Geyer, “Transmission/reflection and short-circuit line methods for measuring permittivity and permeability,” *Nat. Inst. Stand. Technol. Tech. Note*, 1355-R, 1993.